

Topological Maxwell Metal Bands in a Superconducting Qutrit

Xinsheng Tan,¹ Dan-Wei Zhang,² Qiang Liu,¹ Guangming Xue,¹ Hai-Feng Yu,^{1,*} Yan-Qing Zhu,¹ Hui Yan,² Shi-Liang Zhu,^{1,2,3,†} and Yang Yu^{1,3,‡}

¹*National Laboratory of Solid State Microstructures,*

School of Physics, Nanjing University, Nanjing 210093, China

²*Guangdong Provincial Key Laboratory of Quantum Engineering and Quantum Materials, SPTE, South China Normal University, Guangzhou 510006, China*

³*Synergetic Innovation Center of Quantum Information and Quantum Physics, University of Science and Technology of China, Hefei, Anhui 230026, China*

We experimentally explore the topological Maxwell metal bands by mapping the momentum space of condensed-matter models to the tunable parameter space of superconducting quantum circuits. An exotic band structure that is effectively described by the spin-1 Maxwell equations is imaged. Three-fold degenerate points dubbed Maxwell points are observed in the Maxwell metal bands. Moreover, we engineer and observe the topological phase transition from the topological Maxwell metal to a trivial insulator, and report the first experiment to measure the Chern numbers that are higher than one.

Discovery of new states of matter in condensed-matter materials or synthetic systems is at the heart of modern physics [1–3]. The last decade has witnessed a growing interest in engineering quantum systems with novel band structures for topological states, ranging from graphene and topological insulators [1–7], to topological semimetals and metals [8–12]. The band structures of graphene and some topological insulators or semimetals near the two-fold degenerate points simulate relativistic spin-1/2 particles in the quantum field theory described by the Dirac or Weyl equation. Most interestingly, the Dirac and Weyl bands have rich topological features [1–12]. For instance, states in the vicinity of a Weyl point possess a non-zero topological invariant (the Chern number). The topological bands with two-fold degenerate points so far realized simulate conventional Dirac-Weyl fermions studied in the quantum field theory. On the other hand, unconventional bands with topological properties mimicking higher spin counterparts are also fundamentally important but rarely studied in condensed matter physics or artificial systems [13, 14], noting that they provide potentially a quantum family to find quasiparticles that have no high-energy analogs, such as integer-(pseudo)spin fermionic excitations. Recently, a piece of pioneering work in this direction theoretically predicted that new fermions beyond Dirac-Weyl fermions can emerge in some band structures with three- or more-fold degenerate points [13]. The three-fold degeneracies in the bands carry large Chern numbers $C = \pm 2$ and give rise to two chiral Fermi arcs and the spin-1 quasiparticles [13]. The spin-1 particles can exhibit striking relativistic quantum dynamics beyond the Dirac dynamics [1], such as super-Klein tunneling and supercollimation effects [15] and geometrodynamics of spin-1 photons [16]. However, these topological bands with the unconventional fermions have yet been observed in real materials or artificial systems. Several challenges may hinder their experimental investigation in conventional materials and condensed

matter systems. The first is that the realization of the spin-1 Hamiltonian requires unconventional spin-orbital interactions in three-dimensional (3D) periodic lattices [13]. Second, it is difficult to continuously tune the parameters in materials to study fruitful topological properties including topological transition. Moreover, it is difficult to directly detect the topological invariant of the multi-fold degenerate points in condensed matter systems. Nevertheless, artificial superconducting quantum circuits possessing high controllability [17–32] provide an ideal and powerful tool for quantum simulation and the study of novel quantum systems, including the topological ones [30–32].

In this Letter, we experimentally explore an unconventional topological band structure, called Maxwell metal bands, with a superconducting qutrit via an analogy between the momentum space of the presented condensed-matter model and the tunable parameter space of superconducting quantum circuits. By measuring the whole energy spectrum of our system, we clearly image a new band structure, which consists of a flat band and two three-fold degenerate points in the 3D parameter space dubbed Maxwell points. The system dynamics near the Maxwell points are effectively described by the analogous spin-1 Maxwell equations. We further investigate the topological properties of Maxwell metal bands by measuring the Chern numbers ± 2 of the simulated Maxwell points from the non-adiabatic response of the system. By tuning the Hamiltonian parameters, we engineer the topological phase transition from the Maxwell metal to a trivial insulator, which is demonstrated unambiguously from the evolution of tunable band structures and Chern numbers across the critical points.

We realize the following model Hamiltonian in momentum space describing a free pseudospin-1 particle [33]

$$\mathcal{H}(\mathbf{k}) = R_x S_x + R_y S_y + R_z S_z, \quad (1)$$

where $\mathbf{k} = (k_x, k_y, k_z)$ denote the quasimomenta, $R_x =$

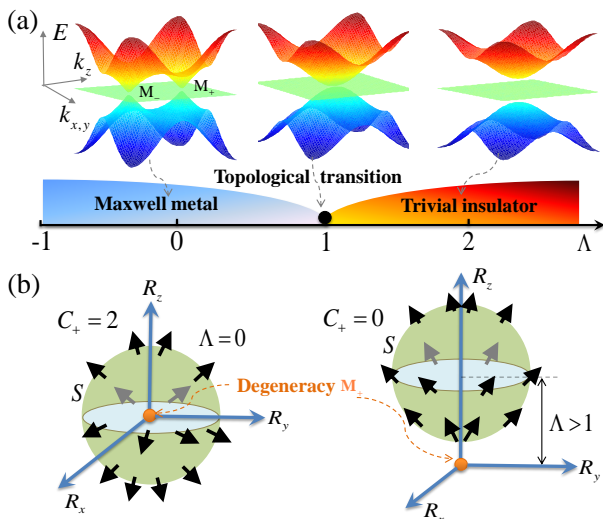


FIG. 1: (Color online) Phase diagram and geometric illustration of the spin-1 Maxwell system. (a) Phase diagram of the Maxwell system with respect to the parameter Λ . From left to right: the energy spectra for the Maxwell metal phase with a pair of Maxwell points denoted by \mathbf{M}_{\pm} ($\Lambda = 0$), the topological transition point with the merging of the two points ($\Lambda = 1$), and the trivial insulator phase with band gaps ($\Lambda = 2$). (b) Geometric illustrations of the topological difference between the two distinct phases when the spherical manifold \mathcal{S} moves from the degeneracy in the z direction by distance Λ . The Berry flux vectors are schematically presented by arrows, showing the different signature textures for the topological and trivial phases: The vectors fully (do not) wind around in the topological (trivial) case with $\Lambda = 0$ ($\Lambda > 1$) giving the Chern number $C_+ = 2$ ($C_+ = 0$).

$\sin k_x$, $R_y = \sin k_y$, and $R_z = \Lambda + 2 - \cos k_x - \cos k_y - \cos k_z$ are the Bloch vectors with a control parameter Λ , and $S_{x,y,z}$ are the spin-1 matrices. The resulting three bands can touch at certain points in the first Brillouin zone for proper Λ with a zero-energy flat band in the middle. For instance, when $|\Lambda| < 1$, the bands host two threefold degeneracy points at $\mathbf{M}_{\pm} = (0, 0, \pm \arccos \Lambda)$. Near \mathbf{M}_{\pm} one has the low-energy effective Hamiltonian

$$\mathcal{H}_{\pm}(\mathbf{q}) = q_x S_x + q_y S_y \pm \alpha q_z S_z, \quad (2)$$

with $\alpha = \sqrt{1 - \Lambda^2}$ and $\mathbf{q} = \mathbf{k} - \mathbf{M}_{\pm}$ for the two degeneracy points. Equation (2) is analogous to the Maxwell Hamiltonian for photons and the dynamics of the low-energy pseudospin-1 excitations are effectively described by the Maxwell equations [34, 35]. In this sense, the threefold degeneracy points are named Maxwell points, similar to the Dirac and Weyl points in some (pseudo)spin-1/2 systems, such as graphene and Weyl semimetals [1–11].

The spin-1 system described by Hamiltonian (1) has two different topological phases determined by the parameter Λ : the topological Maxwell metal phase with a pair of Maxwell points in the bands when $|\Lambda| < 1$ and the

trivial insulator phase with band gaps when $|\Lambda| > 1$. At the critical point $\Lambda = 1$, the two Maxwell points merge and then disappear at the band center, indicating the topological transition. The phase diagram and typical band structures are illustrated in Fig. 1(a) ($\Lambda = 0, 1, 2$ from left to right). The topological nature of Maxwell metal bands can be revealed from the two Maxwell points acting as the sink and source of the Berry flux in 3D momentum or parameter space. Moreover, the topological invariant of the Maxwell points \mathbf{M}_{\pm} is given by the Chern numbers C_{\pm} defined as the integral over a closed manifold \mathcal{S} in the momentum or parameter space of \mathcal{H}_{\pm}

$$C_{\pm} = \frac{1}{2\pi} \oint_{\mathcal{S}} \mathbf{F}_{\pm} \cdot d\mathbf{S} = \pm 2, \quad (3)$$

where \mathbf{F}_{\pm} denote the vector form of the Berry curvature [33]. Hence, the transition between the two distinct phases can be topologically represented by the movement of a spherical manifold \mathcal{S} of radius 1 from the degeneracy in the z direction by distance Λ , as shown in Fig. 1(b). When $|\Lambda| < 1$ the degeneracy lies within \mathcal{S} , giving $C_{\pm} = 2$ for the Maxwell metal phase; when $|\Lambda| > 1$ it lies outside \mathcal{S} , giving $C_{\pm} = 0$ for the trivial insulator phase.

Below we simulate the Hamiltonian (1) with a fully controllable artificial superconducting qutrit. The sample used in our experiment is a 3D transmon, which consists of a superconducting qutrit embedded in a 3D aluminium cavity [36] of which TE101 mode is at 9.053 GHz. The intrinsic quality factor of the cavity is about 10^6 . The whole sample package is cooled in a dilution refrigerator to a base temperature of 30 mK. Fig. 2(a) is a brief schematic of our experimental setup for manipulating and measuring the 3D transmon (see Supplementary Information). The principals of manipulation and measurement for a 3D transmon are based on the theory of circuit QED [37, 38], which describes the interaction of artificial atoms subject to microwave fields. We designed the energy levels of the transmon to make the system work in the dispersive regime.

In general, the transmon has multiple energy levels and we use the four lowest ones denoted as $|0\rangle$, $|1\rangle$, $|2\rangle$, and $|3\rangle$. Here $\{|1\rangle, |2\rangle, |3\rangle\}$ form the qutrit basis and are used to simulate the model Hamiltonian of the Maxwell system, and $|0\rangle$ is set as a reference level for measuring spectrum [Fig. 2(b)]. First, we calibrated the transmon. The transition frequencies between different energy levels are $\omega_{01}/2\pi = 7.17133$ GHz, $\omega_{12}/2\pi = 6.8310$ GHz and $\omega_{23}/2\pi = 6.4470$ GHz, which are independently determined by saturation spectroscopies. The energy relaxation times of the transmon are $T_1^{01} \sim 15 \mu\text{s}$, $T_1^{12} \sim 12 \mu\text{s}$ and $T_1^{23} \sim 10 \mu\text{s}$. The dephasing times are $T_2^{*01} \sim 4.3 \mu\text{s}$, $T_2^{*12} \sim 3.5 \mu\text{s}$ and $T_2^{*23} \sim 3.0 \mu\text{s}$. In order to obtain the spin-1 Hamiltonian [Eq. (4)], as shown in Fig. 2(b), we apply microwave fields with frequencies ω_{12} , ω_{13} and ω_{23} to generate transitions between the three levels, respectively denoted as R_z , R_y and R_x . These transitions are

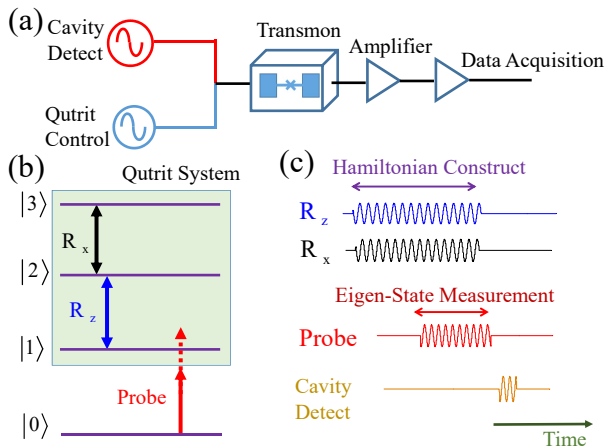


FIG. 2: (Color online) Experimental setup. (a) Schematic of experimental setup for controlling and measuring a 3D superconducting transmon qutrit. The microwaves for manipulating and measuring the qutrit are applied to the sample. We use digital heterodyne for data acquisition. Amplifiers and filters are used to increase signal-to-noise ratio and isolate qutrit from external noise. (b) Schematic of the relevant energy levels of the transmon for spectroscopy measurement. Levels $|1\rangle$, $|2\rangle$, and $|3\rangle$ form the spin-1 basis $\{(1, 0, 0)^T, (0, 1, 0)^T, (0, 0, 1)^T\}$. $|0\rangle$ serves as the reference level to measure the spectroscopy by sweeping the frequency of the probe microwave (schematically illustrated by the dashed arrow). (c) Time profile for spectroscopy measurement. The control microwave pulses R_z and R_x drive the system to form the eigenstates, which are empty. Then the probe microwave pulse pumps the system from $|0\rangle$ to the eigenstates when its frequency matches the level spacing. By sending a detect pulse to the cavity, we can readout the population in the eigenstates as resonant peaks. By collecting the resonant peaks we obtain the energy spectrum of the Maxwell metal.

equivalent to the rotations with respect to different axes. IQ mixers combined with arbitrary wave generators are used to control the amplitude, frequency, and phase of microwave pulses. For the microwave-driven qutrit system, the Hamiltonian with a tunable parameter \mathbf{k} under rotating wave approximation can be written as

$$H(\mathbf{k}) = \begin{pmatrix} 0 & -i\Omega_{12}/2 & i\Omega_{13}/2 \\ i\Omega_{12}/2 & 0 & -i\Omega_{23}/2 \\ -i\Omega_{13}/2 & i\Omega_{23}/2 & 0 \end{pmatrix} + \omega_{01}\mathbf{I}_{3\times 3}. \quad (4)$$

Here we design the transition rates as $\{\Omega_{23}, \Omega_{13}, \Omega_{12}\} = \{R_x, R_y, R_z\}$ to mimic the model Hamiltonian in the parameter space, and $\mathbf{I}_{3\times 3}$ is the 3 by 3 unit matrix. Diagonalizing $H(\mathbf{k})$ yields three eigenstates $|0_d\rangle$ and $|\pm\rangle$, with the corresponding eigen energies $E_0 = \omega_{01}$ as the flat band and $E_{\pm} = \omega_{01} \pm \sqrt{R_x^2 + R_y^2 + R_z^2}$ as the upper and lowest bands shown in Fig. 1(a).

We directly measure the spectroscopy of the driven transmon and obtain the band structure of $H(\mathbf{k})$. Without loss of generality, we always set $k_y = 0$ in the band-

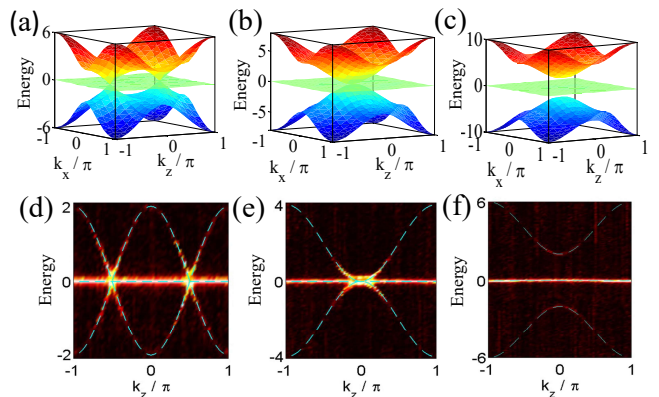


FIG. 3: (Color online) Measuring Maxwell bands. (a,b,c) The measured band structures in the first Brillouin zone for various Λ show different topological properties. (d,e,f) show the cross sections of band structures containing Maxwell points in $E-k_z$ plane, where a linear dispersion is clear in the Maxwell metal phase. From (a) to (c) [from (d) to (f)], $\Lambda = 0, 1, 2$, respectively. The experimental data (colored dots) and theoretical calculations (blue dashed lines) agree well with each other. The spectra are plotted by dropping the overall energy constant ω_{01} with the energy unit $\Omega = 15$ MHz.

structure measurement. For given k_x and k_z , the driving microwaves construct the eigenstates $|0_d\rangle$ and $|\pm\rangle$. A probe microwave pulse is used to pump the system from $|0\rangle$ to the eigenstates and the resonant peaks of microwave absorption are detected [33]. By mapping the frequency of the resonant peak as a function of k_x and k_z , we extract the entire band structure over the first Brillouin zone, as illustrated from Fig. 3a to 3c, which agree well with the theoretical results shown in Fig. 1(a). The topological properties of the spin-1 Maxwell system depend on Λ . For $\Lambda = 0$ [Fig. 3(a)], the system is in the Maxwell metal phase and two Maxwell points located at $(0, \pm\pi/2)$ in k_x-k_z plane are observed. When Λ increases to 1 [Fig. 3(b)], two Maxwell points merge at $(0, 0)$, indicating the topological phase transition. They then completely disappear with further increase of Λ and the system becomes a trivial insulator, as shown in Fig. 3(c) ($\Lambda = 2$). Furthermore, the measured cross section of the Maxwell points in the $E-k_z$ plane with $k_x = 0$ in Figs. 3(d,e,f) agree well with the theoretical results. This clearly indicates the evolution of the dispersion from the linear one (thus the quasiparticles are relativistic) near the Maxwell points with a flat band to the quadratic one when crossing the transition point.

We detect the Chern numbers of the Maxwell points by dynamically measuring the Berry curvature in the parameter space from the non-adiabatic response in the quasi-adiabatic procedure [Fig. 4(a)]. This non-adiabatic approach [39] has been shown to be a convenient way to measure the Berry curvature of a spin-1/2 system [30, 31]. We here demonstrate that it can be generalized to a spin-1 system. Since the probe level is no longer needed in

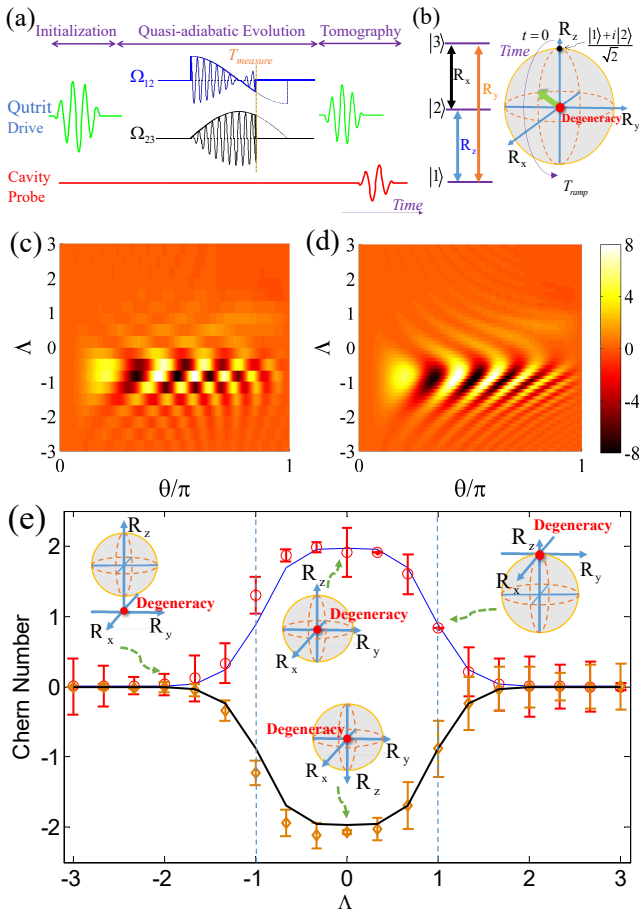


FIG. 4: (Color online) Dynamically measuring the Chern numbers of the Maxwell points and the topological transition. (a) Time profile for the measurement of Chern number. The qutrit state is initialized at $(|1\rangle + i|2\rangle)/\sqrt{2}$ and then evolves quasi-adiabatically during a non-adiabatic ramp, which is followed by state tomography. (b) Three lowest energy levels $\{|1\rangle, |2\rangle, |3\rangle\}$ coupled by pluses $R_{x,y,z}$ are used to construct the spin-1 Hamiltonian, and the pulse sequence results in a parameter-space motion along the $\phi = 0$ meridian ($R_y = 0$) on the spherical manifold. (c) and (d) The measured and simulated (with the measured decoherence time of the transmon) Berry curvature $F_{\theta\phi}$ as functions of θ and Λ . The oscillation pattern suggests a non-adiabatic response. (e) The measured (circles and diamonds) and simulated (solid line) Chern numbers as a function of Λ for the Maxwell points. For $|\Lambda| < 1$, $|C_{\pm}| = 2$ indicates the Maxwell points in the topological Maxwell metal phase; for $|\Lambda| > 1$, $|C_{\pm}| = 0$ indicates the system in the trivial insulator phase.

this measurement, we select the lowest three levels in the superconducting transmon [Fig. 4(b)], labeled still as $\{|1\rangle, |2\rangle, |3\rangle\}$ for consistent definitions in equations). We choose $\{\Omega_{23}, \Omega_{13}, \Omega_{12}\} = \{\sin\theta \cos\phi, \sin\theta \sin\phi, \cos\theta + \Lambda\}$ to realize the spherical manifold enclosing \mathbf{M}_+ [Fig. 4(b)], where $\theta \in [0, \pi]$ and $\phi \in [0, 2\pi]$ are spherical coordinates. We consider the parameter trajectory that starts at the north pole by preparing the initial qutrit state

$(|1\rangle + i|2\rangle)/\sqrt{2}$, which is the eigenstate of the S_z operator. We then linearly ramp the angle θ as a function $\theta(t) = \pi t/T_{\text{ramp}}$ along the $\phi = 0$ meridian in Fig. 4b. Finally we stop the ramp at various times $t_{\text{measure}} \in [0, T_{\text{ramp}}]$ and perform tomography of the qutrit state. In the adiabatic limit, the system will remain in the meridian. However, we use quasi-adiabatic ramps with fixed $T_{\text{ramp}} = 600$ ns $\sim \Omega/10$ ($\Omega = 15$ MHz is the energy unit), and the local Berry curvature introduces a deviation from the meridian, which can be defined as the generalized force [33] $\langle M_\phi \rangle = -\langle \partial_\phi H(\theta, \phi) \rangle|_{\phi=0} = \langle S_y \rangle \sin\theta$. Then at each t_{measure} , we extract the Berry curvature $F_{\theta\phi} \approx \langle M_\phi \rangle / v_\theta$ from the measured values of $\langle S_y \rangle$, where $v_\theta = \pi/T_{\text{ramp}}$ is the ramp velocity. As the Hamiltonian is cylindrically invariant around the z axis, a line integral is sufficient for measuring the surface integral of the Chern number as $C = \int_0^\pi F_{\theta\phi} d\theta$. We extract $F_{\theta\phi}$ of the two Maxwell points \mathbf{M}_\pm for $\Lambda = 0$ and obtain the Chern numbers $C_+ = 1.98 \pm 0.34$ and $C_- = -2.14 \pm 0.05$, which are close to the theoretical values ± 2 .

To investigate the topological phase transition in the transmon, we measure $F_{\theta\phi}$ of \mathbf{M}_\pm as a function of θ and the tunable parameter Λ . The measured $F_{\theta\phi}$ of \mathbf{M}_+ [Fig. 4(c)] is in good agreement with the result of numerical simulations [Fig. 4(d)]. At $\Lambda = 0$, the manifold of the spherical parameter space contains degeneracy at the center [Fig. 4(b)], indicating that the simulated Hamiltonian is in the Maxwell metal phase and the extracted Chern numbers $|C_\pm| \approx 2$. Moving degeneracy along R_z axis by varying Λ [as illustrated in Fig. 4(e)] is equivalent to deforming the manifold in the language of topology. When $|\Lambda| < 1$, $|C_\pm| \approx 2$ indicates that the degeneracy still lies inside spherical manifold. When the degeneracy is moving outside the parameter sphere for $|\Lambda| > 1$, $|C_\pm| \approx 0$ indicates that the system becomes a trivial insulator. Hence, topological phase transitions occur at $|\Lambda| = 1$, where C_\pm will jump between discrete values. Our measurements capture essential features of the theoretical prediction [Fig. 4(e)]. It is noticed that the transition of C_\pm is not abrupt at the critical points, which is mainly due to the finite decoherence time of the transmon. The simulation results (solid line) by considering the decoherence time of the transmon agree well with the experimental data [33].

In summary, we have explored essential physics of the momentum space Hamiltonian corresponding to topological Maxwell metal bands with a superconducting qutrit, which can be generalized to other artificial systems, including photonic crystals [11, 12] and trapped ions [40]. A next study in this Maxwell system is to simulate complex relativistic quantum dynamics of spin-1 particles beyond the Dirac dynamics [1], such as super-Klein tunneling [15] and double-Zitterbewegung oscillations. By using more energy levels in the superconducting artificial atom, one can emulate topological bands with higher-spin relativistic dispersions, such as spin-3/2 Rarita-

Schwinger-Weyl semimetals [14]. Furthermore, by coupling individual superconducting qutrits properly, one can extend the system to explore the topological phase transition induced by the qutrit-qutrit interaction, similar to that observed in the qubit-qubit interacting system [31], even in principle, to implement the celebrated topological Haldane phase of interacting spin-1 quantum chain [41].

This work was supported by the NKRDP of China (Grant No. 2016YFA0301800), the NSFC (Grants No. 11604103, No. 11474153, and No. 91636218), the NSF of Guangdong Province (Grant No. 2016A030313436), and the Startup Foundation of SCNU.

X. T. and D.-W. Z contributed equally to this work.

* Electronic address: hfyu@nju.edu.cn

† Electronic address: slzhu@nju.edu.cn

‡ Electronic address: yuyang@nju.edu.cn

- [1] A. H. Castro Neto, F. Guinea, N. M. R. Peres, K. S. Novoselov, and A. K. Geim, The electronic properties of graphene, *Rev. Mod. Phys.* **81**, 109 (2009).
- [2] M. Z. Hasan and C. L. Kane, Topological insulators, *Rev. Mod. Phys.* **82**, 3045 (2010).
- [3] X. L. Qi and S. C. Zhang, Topological insulators and superconductors, *Rev. Mod. Phys.* **83**, 1057 (2011).
- [4] L. Tarruell, D. Greif, T. Uehlinger, G. Jotzu, and T. Esslinger, Creating, moving and merging Dirac points with a Fermigas in a tunable honeycomb lattice, *Nature (London)* **483**, 302 (2012).
- [5] S. L. Zhu, B. G. Wang, and L. M. Duan, Simulation and detection of Dirac fermions with cold atoms in an optical lattice, *Phys. Rev. Lett.* **98**, 260402 (2007).
- [6] L. Duca, T. Li, M. Reitter, I. Bloch, M. Schleier-Smith, and U. Schneider, An Aharonov-Bohm interferometer for determining Bloch band topology, *Science* **347**, 288 (2015).
- [7] M. Aidelsburger, M. Lohse, C. Schweizer, M. Atala, J. T. Barreiro, S. Nascimbène, N. R. Cooper, I. Bloch, and N. Goldman, Measuring the Chern number of Hofstadter bands with ultracold bosonic atoms, *Nat. Phys.* **11**, 162 (2015).
- [8] X. Wan, A. M. Turner, A. Vishwanath, and S. Y. Savrasov, Topological semimetal and Fermi-arc surface states in the electronic structure of pyrochlore iridates, *Phys. Rev. B* **83**, 205101 (2011).
- [9] S. Y. Xu, I. Belopolski, N. Alidoust, M. Neupane, G. Bian, C. Zhang, R. Sankar, G. Chang, Z. Yuan, C. C. Lee, S. M. Huang, H. Zheng, J. Ma, D. S. Sanchez, B. Wang, A. Bansil, F. Chou, P. P. Shibayev, H. Lin, S. Jia, and M. Z. Hasan, Discovery of a Weyl fermion semimetal and topological Fermi arcs, *Science* **349**, 613 (2015).
- [10] B. Q. Lv, H. M. Weng, B. B. Fu, X. P. Wang, H. Miao, J. Ma, P. Richard, X. C. Huang, L. X. Zhao, G. F. Chen, Z. Fang, X. Dai, T. Qian, and H. Ding, Experimental discovery of Weyl semimetal TaAs, *Phys. Rev. X* **5**, 031013 (2015).
- [11] L. Lu, Z. Wang, D. Ye, L. Ran, L. Fu, J. D. Joannopoulos, and M. Soljačić, Experimental observation of Weyl points, *Science* **349**, 622 (2015).
- [12] W. J. Chen, M. Xiao, and C. T. Chan, Photonic crystals possessing multiple Weyl points and the experimental observation of robust surface states, *Nat. Commun.* **7**, 13038 (2016).
- [13] B. Bradlyn, J. Cano, Z. Wang, M. G. Vergniory, C. Felser, R. J. Cava, and B. A. Bernevig, Beyond Dirac and Weyl fermions: Unconventional quasiparticles in conventional crystals, *Science* **353**, 5037 (2016).
- [14] L. Liang and Y. Yu, Rarita-Schwinger-Weyl semimetal in $J_{\text{eff}} = 3/2$ electron systems, *Phys. Rev. B* **93**, 045113 (2016).
- [15] A. Fang, Z. Q. Zhang, S. G. Louie, and C. T. Chan, Klein tunneling and supercollimation of pseudospin-1 electromagnetic waves, *Phys Rev B* **93**, 035422 (2016).
- [16] K. Y. Bliokh, A. Niv, V. Kleiner, and E. Hasman, Geometrodynamics of spinning light, *Nat. Photon.* **2**, 748 (2008).
- [17] J. Q. You and F. Nori, Atomic physics and quantum optics using superconducting circuits. *Nature (London)* **474**, 589 (2011).
- [18] A. A. Abdumalikov, J. M. Fink, K. Juliusson, M. Pechal, S. Berger, A. Wallraff, and S. Filipp, Experimental realization of non-Abelian non-adiabatic geometric gates, *Nature (London)* **496**, 482 (2013).
- [19] X. Tan, D.-W. Zhang, Z. Zhang, Y. Yu, S. Han, and S.-L. Zhu, Demonstration of geometric Landau-Zener interferometry in a superconducting qubit, *Phys. Rev. Lett.* **112**, 027001 (2014).
- [20] M. S. Allman, J. D. Whittaker, M. Castellanos-Beltran, K. Cicak, F. da Silva, M. P. DeFeo, F. Lecocq, A. Sirois, J. D. Teufel, J. Aumentado, and R. W. Simmonds, Tunable resonant and nonresonant interactions between a phase qubit and LC resonator, *Phys. Rev. Lett.* **112**, 123601 (2014).
- [21] K. Inomata, K. Koshino, Z. R. Lin, W. D. Oliver, J. S. Tsai, Y. Nakamura, and T. Yamamoto, Microwave down-conversion with an impedance-matched Λ system in driven circuit QED, *Phys. Rev. Lett.* **113**, 063604 (2014).
- [22] K. W. Murch, S. J. Weber, C. Macklin, and I. Siddiqi, Observing single quantum trajectories of a superconducting quantum bit, *Nature (London)* **502**, 211 (2013).
- [23] C. M. Wilson, G. Johansson, A. Pourkabirian, M. Simoen, J. R. Johansson, T. Duty, F. Nori, and P. Delsing, Observation of the dynamical Casimir effect in a superconducting circuit. *Nature (London)* **479**, 376 (2011).
- [24] G. J. Grabovskij, T. Peichl, J. Lisenfeld, G. Weiss, and A. V. Ustinov, Strain tuning of individual atomic tunneling systems detected by a superconducting qubit, *Science* **338**, 232 (2012).
- [25] A. D. Corcoles, E. Magesan, S. Srinivasan, A. W. Cross, M. Steffen, J. M. Gambetta, and J. M. Chow, Demonstration of a quantum error detection code using a square lattice of four superconducting qubits, *Nat. Commun.* **6**, 6979 (2015).
- [26] M. Stern, G. Catelani, Y. Kubo, C. Grezes, A. Bienfait, D. Vion, D. Esteve, and P. Bertet, Flux qubits with long coherence times for hybrid quantum circuits, *Phys. Rev. Lett.* **113**, 123601 (2014).
- [27] C. Deng, J. L. Orgiazzi, F. Shen, S. Ashhab, and A. Lupascu, Observation of floquet states in a strongly driven artificial atom, *Phys. Rev. Lett.* **115**, 133601 (2015).
- [28] Z. Kim, B. Suri, V. Zaretsky, S. Novikov, K. D. Osborn,

- A. Mizel, F. C. Wellstood, and B. S. Palmer, Decoupling a Cooper-pair box to enhance the lifetime to 0.2 ms, *Phys. Rev. Lett.* **106**, 120501 (2011).
- [29] G. Sun, X. Wen, M. Bo, C. Jian, Y. Yang, P. Wu, and S. Han, Tunable quantum beam splitters for coherent manipulation of a solid-state tripartite qubit system, *Nat. Commun.* **1**, 51 (2010).
- [30] M. D. Schroer, M. H. Kolodrubetz, W. F. Kindel, M. Sandberg, J. Gao, M. R. Vissers, D. P. Pappas, A. Polkovnikov, and K. W. Lehnert, Measuring a topological transition in an artificial spin-1/2 system, *Phys. Rev. Lett.* **113**, 050402 (2014).
- [31] P. Roushan, C. Neill, Y. Chen, M. Kolodrubetz, C. Quintana, N. Leung, M. Fang, R. Barends, B. Campbell, Z. Chen, et al., Observation of topological transitions in interacting quantum circuits, *Nature (London)* **515**, 241 (2014).
- [32] X. Tan, Y. X. Zhao, Q. Liu, G. Xue, H. Yu, Z. D. Wang, and Y. Yu, Realizing and manipulating space-time inversion symmetric topological semimetal bands with superconducting quantum circuits, arXiv:1702.01512
- [33] See Supplemental Material for theoretical and experimental details.
- [34] Y. Q. Zhu, D.-W. Zhang, H. Yan, D. Y. Xing, and S. L. Zhu, Maxwell quasiparticles emerged in optical lattices, arXiv:1610.05993.
- [35] M. Stone, Berry phase and anomalous velocity of Weyl fermions and Maxwell photons, *Int. J. Mod. Phys. B* **30**, 1550249 (2016).
- [36] H. Paik, D. I. Schuster, L. Bishop, G. Kirchmair, G. Catelani, A. Sears, B. R. Johnson, M. Reagor, L. Frunzio, and L. I. Glazman, Observation of high coherence in Josephson junction qubits measured in a three-dimensional circuit QED architecture. *Phys. Rev. Lett.* **107**, 240501 (2011).
- [37] A. Blais, R. S. Huang, A. Wallraff, S. M. Girvin, and R. J. Schoelkopf, Cavity quantum electrodynamics for superconducting electrical circuits: An architecture for quantum computation, *Phys. Rev. A* **69**, 062320 (2004).
- [38] M. D. Reed, L. DiCarlo, B. R. Johnson, L. Sun, D. I. Schuster, L. Frunzio, and R. J. Schoelkopf, High-fidelity readout in circuit quantum electrodynamics using the Jaynes-Cummings nonlinearity, *Phys. Rev. Lett.* **105**, 173601 (2010).
- [39] V. Gritsev and A. Polkovnikov, Dynamical quantum Hall effect in the parameter space, *Proc. Natl Acad. Sci. USA* **109**, 6457 (2012).
- [40] R. Gerritsma, G. Kirchmair, F. Zähringer, E. Solano, R. Blatt, and C. F. Roos, Quantum simulation of the Dirac equation. *Nature (London)* **463**, 68 (2010).
- [41] F. D. M. Haldane, Nonlinear field theory of large-spin Heisenberg antiferromagnets: Semiclassically quantized solitons of the one-dimensional easy-axis Néel state, *Phys. Rev. Lett.* **50**, 1153 (1983).